

A Systematic Chandra study of Sgr A^{*}: I. X-ray flare detection

Qiang Yuan* and Q. Daniel Wang†

Department of Astronomy, University of Massachusetts, 710 North Pleasant St., Amherst, MA, 01003, U.S.A.

24 November 2015

ABSTRACT

Daily X-ray flaring represents an enigmatic phenomenon of Sgr A^{*} — the supermassive black hole at the center of our Galaxy. We report initial results from a systematic X-ray study of this phenomenon, based on extensive *Chandra* observations obtained from 1999 to 2012, totaling about 4.5 Ms. We detect flares, using a combination of the maximum likelihood and Markov Chain Monte Carlo methods, which allow for a direct accounting for the pile-up effect in the modeling of the flare lightcurves and an optimal use of the data, as well as the measurements of flare parameters, including their uncertainties. A total of 82 flares are detected. About one third of them are relatively faint, which were not detected previously. The observation-to-observation variation of the quiescent emission has an average root-mean-square of 6% – 14%, including the Poisson statistical fluctuation of faint flares below our detection limits. We find no significant long-term variation in the quiescent emission and the flare rate over the 14 years. In particular, we see no evidence of changing quiescent emission and flare rate around the pericenter passage of the S2 star around 2002. We show clear evidence of a short-term clustering for the ACIS-S/HETG 0th-order flares on time scale of 20 – 70 ks. We further conduct detailed simulations to characterize the detection incompleteness and bias, which is critical to a comprehensive follow-up statistical analysis of flare properties. These studies together will help to establish Sgr A^{*} as a unique laboratory to understand the astrophysics of prevailing low-luminosity black holes in the Universe.

Key words: Galaxy: center — methods: data analysis — accretion, accretion disks — X-rays: individual (Sgr A^{*})

1 INTRODUCTION

Sagittarius A^{*} (Sgr A^{*}), the supermassive black hole (SMBH) at the center of our own Galaxy, is an ideal and unique example to study the accretion of matter onto a black hole (BH). The proximity of Sgr A^{*} enables us to have spatially resolved studies which can hardly be achieved for other SMBHs (e.g., Baganoff et al. 2003; Wang et al. 2013). The pure hot phase of the accretion flow (Yuan & Narayan 2014) makes the relevant physics simple and largely scalable, allowing for an in-depth study with reasonable certainty. Sgr A^{*} also represents a limiting case of low luminosity SMBHs. The study of Sgr A^{*} could then be very useful in understanding this entire class of SMBHs.

The X-ray emission provides very useful diagnostics of the gas inflow/outflow around an SMBH, as well as its interplay with the circum-nuclear environment. The X-ray emission from Sgr A^{*} consists of two components, the extended quiescent emission and hour-scale flares that occur on average a couple of times a day, although the decomposition between the two is still somewhat uncertain (e.g., Baganoff et al. 2001, 2003; Melia & Falcke 2001; Wang et al. 2013).

Since the launch of the *Chandra* X-ray Observatory in 1999, Sgr A^{*} has been monitored frequently, and dozens of flares have been detected (e.g., Baganoff et al. 2001; Eckart et al. 2004, 2006a; Marrone et al. 2008; Yusef-Zadeh et al. 2008). In particular, a *Chandra* X-ray Visionary Project (XVP) was recently carried out for Sgr A^{*} with a total exposure of 3 Ms (Nowak et al. 2012). Spectral analyses of the data from the project suggest that the quiescent component can be well explained by the primarily thermal emission from a radiatively inefficient accretion flow together with an outflow of a similar mass rate (Yuan, Quataert & Narayan 2003, 2004; Wang et al. 2013). Using the data, Neilsen et al. (2013, hereafter N13) detect 39 flares. Flares have also been detected in observations made with other X-ray observatories such as *XMM-Newton* (Porquet et al. 2003; Bélanger et al. 2005; Porquet et al. 2008), *Swift* (Degenaar et al. 2013), and *NuSTAR* (Barrière et al. 2014). The suggested radiation mechanisms of X-ray flares include synchrotron (Yuan, Quataert & Narayan 2003, 2004; Dodds-Eden et al. 2009), inverse Compton scattering (Markoff et al. 2001; Yuan, Quataert & Narayan 2003; Eckart et al. 2004, 2006a; Liu, Melia & Petrosian 2006), and bremsstrahlung (Liu & Melia 2002). In addition, flares have been observed in near-infrared (NIR) observations (Genzel et al. 2003; Dodds-Eden et al. 2009; Trap et al. 2011; Witzel et al. 2012). The strong polarization

* E-mail: yuanq@umass.edu

† E-mail: wqd@astro.umass.edu

of the NIR flare emission indicates a synchrotron origin, and hence the generation of non-thermal electrons (Eckart et al. 2006b).

Two typical dynamical scenarios have been proposed to account for the production of flares. One is the production of hot spots or episodic mass ejections in the accretion flow and/or jets, due to the magnetic reconnection or other magnetohydrodynamical process (e.g., Markoff et al. 2001; Yuan, Quataert & Narayan 2004; Liu, Petrosian & Melia 2004; Yuan et al. 2009; Dodds-Eden et al. 2010). The other is the tidal disruptions of approaching planetesimals by the SMBH (e.g., Kostić et al. 2009; Zubovas, Nayakshin & Markoff 2012). In particular, the comparison of the flare statistics with the theoretical expectation of the so-called self-organized criticality (SOC) system (Katz 1986; Bak, Tang & Wiesenfeld 1987) suggests that the spatial dimension responsible for the production of the flares is $S = 3$, which is similar to that for solar flares and further implies a magnetic reconnection origin of the X-ray flares (Wang et al. 2015; Li et al. 2015). Nevertheless, the exact physical nature of the Sgr A* flares, both the radiation mechanism and the power source, remains unclear (Yuan & Narayan 2014).

In this work, we present a systematic study of the X-ray variabilities of Sgr A*, based on all relevant *Chandra* observations taken from 1999 to 2012. The observations after 2012 are not included in the present study due to the strong confusion from the recently appeared bright magnetar SGR J1745-2900, which is only $2.4''$ away from Sgr A* (Kennea et al. 2013). The data we use were also included in the very recent study by Ponti et al. (2015, hereafter P15). However, their emphasis, primarily on the rate of relatively bright flares and its connection to the pericenter passage of the G2 object (Gillessen et al. 2013), is quite different from ours. We here focus on both a systematic detection of the X-ray flares and a good characterization of the detection incompleteness and bias. This approach is very crucial to a statistical study of both flare and quiescent emissions for two main reasons. First, the analysis enables us to have a significant enlargement of the detected sample of the flares. In particular, the 2012 XVP observations of Sgr A* were taken with the Advanced CCD Imaging Spectrometer - Spectroscopy array (ACIS-S) and with the high energy transmission gratings (HETG) inserted. While allowing for both a high spectral resolution view of Sgr A* and a reduced pileup effect (§ 3.2) on bright flares, the instrument combination substantially decreased the effective collecting area and hence limited the sensitivity of the flare detection. All the observations prior to 2012 used the Advanced CCD Imaging Spectrometer - Imaging array (ACIS-I) without gratings, allowing for detection of flares to lower flare fluences. Second, the 1999-2012 coverage of the ACIS-I and -S/HETG observation combination enables us to explore the long-term evolution of the X-ray emission. The recent study of P15 shows an enhancement of the bright flare rate, but with a drop of the moderate flare rate, several months after the pericenter passage of G2 (Gillessen et al. 2013). We extend this study by probing how the emission may be affected by the pericenter passages of the S2 star and G1 cloud in 2001-2002 (Schödel et al. 2002; Pfuhl et al. 2015).

Compared with previous works, we also have several technical improvements in the present analysis. We employ the unbinned photon events to maximize the use of information in the data. The Markov Chain Monte Carlo (MCMC) method is adopted for the likelihood fitting in order to improve the characterization of the model parameters, especially their errors. For example, the uncertainties in flare durations are so far not given, which prevents a rigorous statistical analysis involving this parameter. We also sta-

tistically test the long-term variability and short-term clustering of the flare rate, which were not addressed in previous works.

2 OBSERVATIONS

Sgr A* was observed 46 times (with a total exposure of 1.5 Ms) between 1999 and 2011, with the *Chandra* ACIS-I camera with no grating. During the 2012 XVP campaign, 38 observations were performed using the ACIS-S camera combined with the HETG, reaching a total exposure of 3 Ms. While the ACIS-S/HETG combination yielded high energy resolution data of Sgr A* for the first time, it reduced the 0th order effective area greatly, compared with the ACIS-I instrument, for example, 150 cm^2 versus 320 cm^2 at 5 keV^1 , and especially at energies $\lesssim 4 \text{ keV}$. The basic information of the observations is compiled in Tables 1 and 2.

The data are reduced with the standard analysis tool CIAO (version 4.5), which includes the exclusion of the time intervals of significant background flaring. We extract the events within $1''.25$ circle region centered on Sgr A*, consistent with those used in other similar studies (N13, P15), to minimize the effect from the extended quiescent emission and the background (Wang et al. 2013, supplementary materials). The non-cosmic X-ray event background in such a small region is negligible. We further filter the events within the $2 - 8 \text{ keV}$ channel energy range, as done in N13 and P15. For the 2012 ACIS-S/HETG observations, we adopt only the non-dispersed (0th order) events, different from N13 in which both the 0th and ± 1 st order events were combined. The use of the 0th order data only (ACIS-S/HETG0 hereafter) makes the pileup correction (see below §3.2) more straight-forward and reliable than that of the 0th+1st order data, because the ratio of the non-dispersed to dispersed events depends on their spectra, which could vary from one flare to another and/or within a flare. The flare detection sensitivities of the 0th and 0th+1st events are expected to be comparable².

3 ANALYSIS

3.1 Flare detection methodology

We adopt a maximum likelihood fitting algorithm to detect flares. This algorithm allow us to use primarily the unbinned data to ensure the minimum loss of information, which is especially important for reliable measurements of those flares whose durations are comparable to, or smaller than 300 s, the bin width used in N13. The use of the MCMC method in the fitting (Neal 1993; Gamerman 1997; Mackay 2003) enables us to effectively survey the high-dimensional, correlated space of the model parameters and determine their posterior probability distributions (hence the uncertainties in the flare parameters). The Metropolis-Hastings algorithm is adopted to generate the Markov chains.

¹ http://xcx.harvard.edu/caldb/prop_plan/pimms/

² The 0th to 1st order count rate ratio of a typical flare is roughly 3 : 2 (N13). However, the quiescent count rate (including the background) of the 0th order data used in this work is about 1.9 ks^{-1} , which is about three times smaller than that of the 0th+1st order data ($5.2 - 5.7 \text{ ks}^{-1}$; Neilsen et al. 2015). To reach the same detection significance of a flare, its count rate of the 0th+1st order data needs to be about $\sqrt{5.5/1.9} = 1.7$ times higher than that of the 0th order data only, which is about the same as the flare count rate ratio.

The model used to describe the lightcurve consists of a quiescent³ emission plus a series of flares. We assume a Gaussian profile as an approximation to the lightcurve of a typical flare. With the limited counting statistics of the data, only a few very bright ones show significant deviations from the profile (e.g., Nowak et al. 2012). Detailed treatment of the asymmetric profiles, both individually and statistically, will be given in a future publication. The model lightcurve can then be expressed as

$$f(t) = \kappa + \sum_{i=1}^n G(t; A_i, \sigma_i, t_{0i}), \quad (1)$$

where κ is the quiescent count rate, and $G(t; A_i, \sigma_i, t_{0i}) = \frac{A_i}{\sqrt{2\pi}\sigma_i} \exp[-(t - t_{0i})^2 / 2\sigma_i^2]$ is the Gaussian profile with the total counts (A_i), the peak time (t_{0i}), and the dispersion (σ_i) of the i th flare, and n is the total number of flares in the lightcurve. The pileup effect, which will be described in § 3.2, is applied directly to the model lightcurve. Then the (logarithmic) likelihood function of the unbinned Cash statistic is (Cash 1979)

$$C \equiv -2 \ln \mathcal{L} = 2 \left(E - \sum_{j=1}^N \ln f^{\text{pi}}(t_j) \right), \quad (2)$$

where $f^{\text{pi}}(t)$ is the pileup affected lightcurve, N is the total observed number of photons, E is the expected number of photons according to Eq. (1), t_j is the arrival time of the j th event, and the summation is over all observed events. The likelihood fitting is performed for individual observation separately.

The actual search procedure for flares in the lightcurve of an observation is as follows. We first bin the data with 300 s bins⁴, and then start to search for flares from the highest count rate bins. For each bin with the maximum count rate in the observation, we fit the unbinned data with an initial flare centroid at the bin center. The width σ_i of a flare is restricted to be larger than 100 s during the search for candidates (N13). This helps reduce false detections (see below). We define the *Test Statistic* of a flare, $\text{TS} = C_0 - C$, where C_0 (C) is the C -statistic without (with) this flare (Mattox et al. 1996). If the TS value for one flare is larger than 14, which corresponds to the one-sided 3σ significance for three free parameters⁵, we have a detection. Then we remove the time interval $[t_{0i} - 3\sigma_i, t_{0i} + 3\sigma_i]$, and repeat the above analysis until that no flare has TS value larger than the threshold in the observed lightcurve. Note that this search procedure tends to miss some weak broad flares (e.g., with low peak count rates). However, it also reduces the number of false detections. We employ Monte Carlo simulations to quantify the probability of false detections due to the background fluctuation. Given the false-alarm probability of $p = 0.0015$, we find that the average number of false detections is about 0.6 (1.2) for the ACIS-I (-S/HETG0) data. The estimated number will be moderately higher if the search width of flare candidates is narrower.

The above flare detection, carried out independently from one

observation to another, is not optimal for a few ACIS-I observations with short exposures. For such an observation, the quiescent emission level cannot be tightly constrained, which also limits the sensitivity of the flare detection. However, the quiescent level on average remains very steady over the 12 year period, as is shown in our later analysis (§4.2). Therefore, we re-analyze the data with the quiescent count rate fixed to the average value of 4.86 (1.86) cts ks⁻¹ for the ACIS-I (ACIS-S/HETG0) observations whose quiescent fluxes deviate from the average ones, which are marked with the “fixed” κ in Tables 1 and 2. Such a re-analysis leads to the detection of three additional flares for the ACIS-I observations. These flares are removed in the re-calculation of the κ values of the affected observations.

There may be significant substructures for some bright flares (Nowak et al. 2012, N13). We add additional Gaussian profiles to characterize such substructures or subflares. The criterion to detect a subflare is that its TS value is larger than 8 (2σ) and its 2σ width overlaps with the adjacent’s. The detection is iterated until no more subflare is found. Finally we do a global fitting with all the flares and subflares to obtain their parameters as well as the quiescent count rate. The number of subflares of each flare, N_{sub} , is included in Tables 1 and 2. Fig. 1 shows an example of a complex lightcurve with multi-flares. The lightcurves of all the detected flares together with the best-fitting results are given in the Appendix.

However, subflares could be due to chance overlapping of a flare with other independent ones. For each flare with detected subflares, we estimate the probability that all its subflares are chance overlapping of independent flares as $P = \prod_{i=1}^{N_{\text{sub}}-1} [1 - \exp(-\Delta t_i / \bar{\Delta t})]$, where Δt_i is the time difference between two adjacent subflares and $\bar{\Delta t} = 44.6$ (60.9) ks is the mean separation between two flares (assuming no correlation) averaged over all flares detected in the ACIS-I (ACIS-S/HETG0) data set. The estimated probability is listed in the last columns of Tables 1 and 2. We find that subflares in only about 1/3 of such flares are expected to be due to the chance overlapping with a probability $\gtrsim 5\%$. Therefore, most of our detected subflares should represent intrinsic substructures of the flares and may be studied statistically. However, there is a complication that subflares are detected with different threshold compared with individual flares (lower significance but with higher background from overlapping flares). Therefore, the above probability estimate is somehow uncertain. More detailed analysis may be needed when subflares are studied.

The duration of a flare is defined to contain the fitting 95% (2.5% – 97.5%) integrated counts, which includes subflares if present. The uncertainties in the fluences and durations are calculated from the bootstrapping realized samples of the fitting model lightcurve, which accounts for the correlations among the parameters.

3.2 Pileup effect

For bright flares, one also needs to consider the so-called pileup effect. If two or more photons arrived at the same detection pixel during a single frame integration time (3.2 s for the *Chandra* ACIS observations considered here), they would be detected as a single event with a higher energy. This effect is significant only for the non-dispersed (0th order) counts when their incident rate at a pixel is sufficiently high (i.e., $\Lambda_{\text{in}} \gtrsim \Lambda_{\text{in}}^{\text{th}} \sim 0.02$ cts s⁻¹). We convert the fitting relation between Λ_{in} and the ACIS output count rate Λ_{out}

³ This “quiescent” component represents the sum of the background (X-ray and non-X-ray), as well as the truly quiescent emission and undetectable weak flares of Sgr A*. Throughout the paper we refer this steady component to “quiescent emission”.

⁴ We have tested that the final results are not sensitive to the start bin width adopted for the candidate searches only.

⁵ The distribution of the TS value in the null hypothesis follows $\chi_n^2/2$ with degree of freedom n (Mattox et al. 1996). For $n = 3$ and $\text{TS} = 14$, the false detection probability is $p = 0.0015$, which corresponds to 3σ significance for one-sided normal distribution.

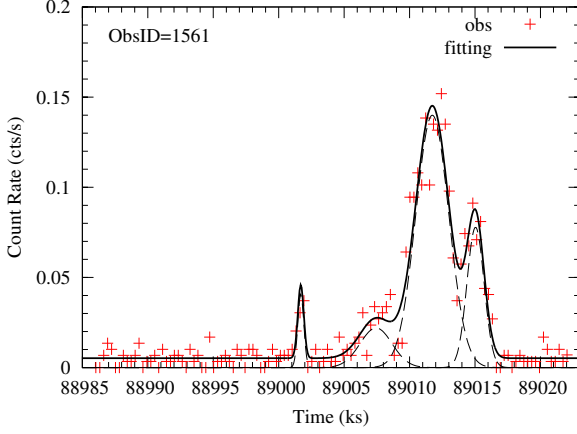


Figure 1. Illustration of a lightcurve, constructed from the data collected in the *Chandra* ACIS-I observation ID 1561 and with a bin size of 300 s (red +; the binning is for the presentation only), compared with the best-fitting model (solid line). Two flares are detected, and the main one consists of three subflares, as shown by the dashed lines.

given in P15 into the following pileup functions:

$$\Lambda_{\text{out}} = \left(4.180\Lambda_{\text{in}}^{-0.07387} + 0.5381\Lambda_{\text{in}}^{-1.160} \right)^{-1}, \quad \text{for ACIS-I,} \quad (3)$$

$$\Lambda_{\text{out}} = \left(3.933\Lambda_{\text{in}}^{-0.03541} + 0.6564\Lambda_{\text{in}}^{-1.107} \right)^{-1}, \quad \text{for ACIS-S/HETG0.} \quad (4)$$

We apply the corresponding pileup function to the parts of the model lightcurve (Eq.(1)) with $\Lambda_{\text{in}} > \Lambda_{\text{in}}^{\text{th}}$, before it is fitted to the observed one. The total incident and pileup-affected fluences for a flare are obtained from integrating its model lightcurve (after subtracting the quiescent emission) before and after the application of the pileup function. The largest pileup correction of the fluence is about 50% for the ACIS-I flares, and about 35% for the ACIS-S/HETG0 flares detected in this analysis (Fig. 2; for the flare parameters, please refer to §4.1). In comparison, the largest correction is $\sim 20\%$ in N13 where the $\pm 1\text{st}$ order data (which suffered no pileup effect) are included, which is broadly consistent with ours taking into account the 0th to 1st order count rate ratio. However, the pileup correction in N13 is applied on an average ACIS-S/HETG 0th+1st order count rate, instead of on the (more directly relevant) ACIS-S/HETG 0th order lightcurve of a flare, as we have done in the present work.

3.3 Detection incompleteness, bias, and uncertainty

With the limited counting statistics, the detection of weak flares can be incomplete and even biased, making the measurements of parameters very uncertain (e.g., Kenter & Murray 2003; Wang 2004). Such uncertainties need to be accounted for when studying the intrinsic properties (such as the flare fluence and duration distributions) of the sample. We characterize the detection incompleteness and bias, as well as the uncertainties of the measured parameters with a redistribution matrix

$$P(F_{\text{det}}, \tau_{\text{det}}; F_{\text{int}}, \tau_{\text{int}}), \quad (5)$$

where the subscriptions “_{det}” and “_{int}” denote the detected and intrinsic parameters.

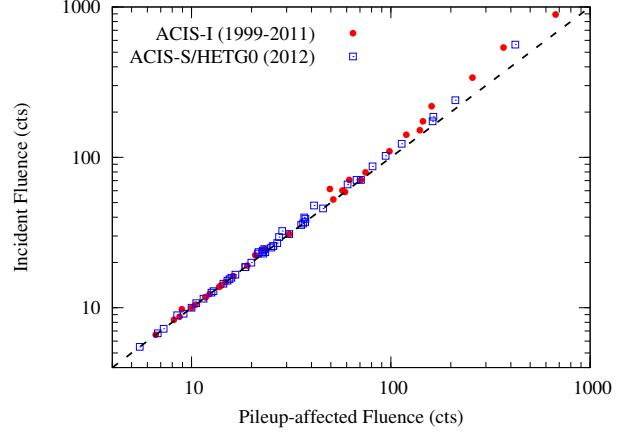


Figure 2. Comparison of the pileup-affected fluences and the calculated incident ones for our detected flares.

We use Monte Carlo simulations to construct the redistribution matrix. Each simulation assumes a quiescent count rate κ and a flare with a fluence F_{int} and a duration τ_{int} , in an observation with a typical exposure of 10^5 s. This flare is randomly inserted in time and assumed to have a Gaussian profile. The arrival time of each photon is randomly generated following the lightcurve Eq. (1). We apply the same flare detection and parameter measurement procedure to the simulated lightcurve as to the real data. If the flare is detected (i.e., with $\text{TS} \geq 14$), then we measure the “detected” parameters F_{det} and τ_{det} . This is repeated for 1000 simulations for each $(F_{\text{int}}, \tau_{\text{int}})$.

Due to the statistical fluctuation, a flare may or may not be detectable above our defined threshold. This detection fraction of simulated flares as a function of the intrinsic fluence and duration is shown in Fig. 3. The left and right panels are for different quiescent rates, which are chosen to mimic those in the ACIS-I and -S/HETG0 observations, respectively. This figure shows that if the fluence is lower than a few tens of counts, the fraction could decrease considerably. The fraction also increases with the flare duration, τ_{int} , the increase of which decreases the signal-to-noise ratio. As illustrated by the 90% fraction contour (long-dashed line in the figure), the incompleteness becomes important even for very high fluence flares when $\tau_{\text{int}} \gtrsim 10^4$ s. This is mainly because such a long-duration flare always has a good chance to be truncated by the start or end of an observation.

The redistribution also determines the detection bias and the uncertainties in the parameter measurements. Fig. 4 illustrates how the parameters (red dots) are redistributed around the input ones (black crosses). The scatters are larger if the fluence is lower and/or the duration is longer (e.g., bottom-right corner). The truncation from bottom-left to top-right for input parameters $(F_{\text{int}}, \tau_{\text{int}}) = (20\text{cts}, 5\text{ks})$ is caused by realizations falling below the detection threshold (see Fig. 3). Conversely, a considerable number of flares which are intrinsically weak could be realized to be above the detected limit. Depending mainly on the steepness of the fluence distribution, the redistribution leads to the so-called Eddington bias: many more flares scattered upwards than downwards (e.g., Wang 2004). The redistribution probabilities, each normalized to the detection fraction for a particular set of the input parameters, are then calculated on logarithmic grids of τ from 0.2 to 20 ks, and of F from 4 to 1000 cts. The resulting 2-D redistribution matrix will enable us to account for the incompleteness and bias of the detection,

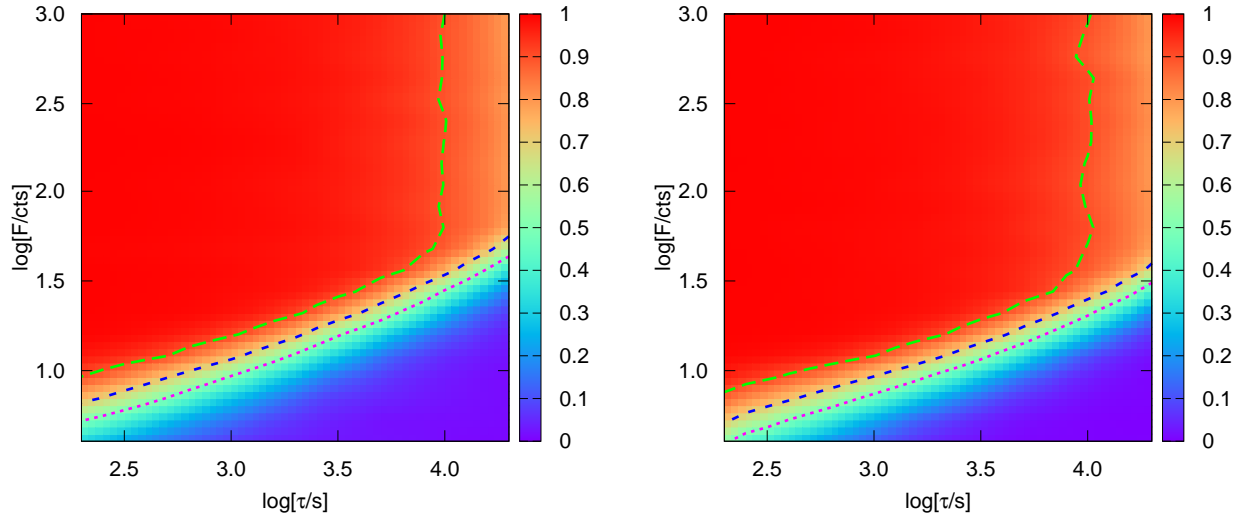


Figure 3. Detection incompleteness as a function of the intrinsic flare fluence and duration. Lines show the 90%, 70%, and 50% iso-contours of the detection fraction from top to bottom. The left panel is for an assumed quiescent rate of 4.9 cts ks^{-1} (similar to ACIS-I data), while the right one for 1.9 cts ks^{-1} (similar to ACIS-S/HETG0 data).

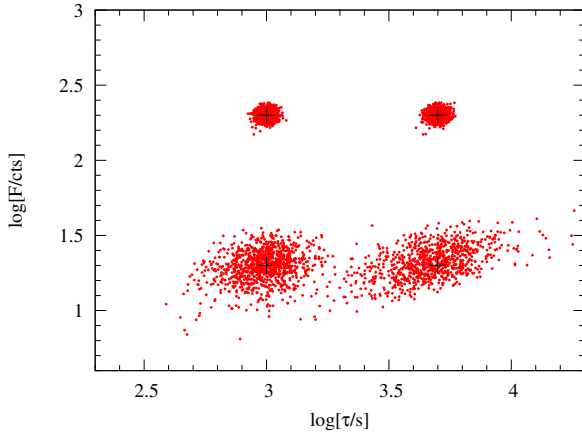


Figure 4. Illustration of measured fluence and duration distributions (red dots) for four sets of simulated flares. The input flare parameters of each set are marked by the black crosses.

as well as the measurement uncertainties of the parameters, critical for a rigorous statistical study of flare properties to be presented in a forthcoming paper.

3.4 Observational gap effect

Large gaps exist between consecutive observations, which need to be accounted for when the rate and waiting time of the flares are analyzed. Some of them were truncated at the start or end of an observation, which affects the detection of such flares (see Fig. 3). The gap effect is especially important for the waiting time analysis because a pair of flares with long enough waiting time will not be detected with a shorter exposure. Under the null hypothesis in

which flares occur randomly, the distribution of the waiting times should be exponential, $dN_{\text{nogap}}/d(\Delta t) \propto \exp(-\Delta t/\bar{\Delta t})$. In case that there are observational gaps, this distribution needs to be modified by a detectable rate, which is an exposure-weighted probability

$$P(\Delta t) = \sum_i H(W_i - \Delta t) \cdot (W_i - \Delta t) / W_{\text{tot}}, \quad (6)$$

where W_i is the exposure of the i th observation, W_{tot} is the sum of all the exposures, $H(W_i - \Delta t)$ is the Heaviside step function, and the sum is over all observations. The term $(W_i - \Delta t)$ in the above equation means that an observation can only have an effective exposure of $(W_i - \Delta t)$ to detect a pair of flares with waiting time Δt . The cumulative distribution of the waiting time is then

$$N_{\text{gap}}(> \Delta t) = \int_{\Delta t}^{\infty} \frac{dN_{\text{nogap}}}{d\Delta t'} \cdot P(\Delta t') d(\Delta t'). \quad (7)$$

We normalize both the expected and the corresponding detected distributions and then calculate the statistic D (the maximum distance between the two distributions) to conduct the Kolmogorov-Smirnov (KS) null hypothesis test.

3.5 Flux and luminosity conversions

To facilitate the comparison of the flare detections based on the observations taken with the two different instrument setups, we convert the count rates of flares into their intrinsic fluxes. This conversion assumes the best-fit power-law model for the accumulated flare spectra presented in Wang et al. (2013, supplementary materials), accounting for the foreground absorption and dust scattering, as well as the pileup effect. The modeling was conducted with the spectral analysis package XSPEC (version 12.8.0; Arnaud 1996). By removing the *multiplicative* pileup model component from this best-fit model, we obtain the conversion from the pileup-free count rate to the absorbed energy flux in the 2–8 keV band as $2.81(7.22) \times 10^{-11} \text{ ergs cm}^{-2} \text{ s}^{-1} / [\text{cts s}^{-1}]$,

for the ACIS-I (-S/HETG0) detected flares. The corresponding count rate to the unabsorbed luminosity conversion is $0.73 (1.88) \times 10^{36} \text{ ergs s}^{-1} / [\text{cts s}^{-1}]$, assuming the distance of Sgr A* to be 8 kpc. The ACIS-I to -S/HETG0 count rate ratio (hence effective area) is about 2.6 for the same incident flux.

4 RESULTS

In total we detect 33 flares in the ACIS-I observations, and 49 flares in the ACIS-S/HETG0 observations. The fitting parameters of these flares and the quiescent emission count rates of individual observations are included in Tables 1 and 2.

4.1 Flare fluences and durations

Fig. 5 shows the fluence-duration distributions of the detected flares, for the ACIS-I (left) and -S/HETG0 (right) observations, as well as those detected in P15 and N13 for comparison. The fluence (in cts) of a P15 flare is obtained through dividing the reported value (in erg cm^{-2}) by the conversion factor $4.2 \times 10^{-11} \text{ (erg cm}^{-2} / \text{cts)}$. In order to have a direct comparison of our sample with that of N13, we multiply the fluences of N13 flares by a factor of ~ 0.6 to account for the 0th to 0th+1st order event ratio, and then apply the pileup function as presented in P15 (the inverse of Eq. (4)) to the flare profiles to calculate the pileup corrected fluences. We find most of the flares that appear above or just around the 50% incompleteness curve are missed in P15 and N13 (see further discussion in §5).

A correlation between the flare fluences and durations is apparent in Fig. 5. We characterize this correlation with a linear function

$$\log(F/\text{cts}) = \log(\alpha) + \beta \log(\tau/\text{ks}). \quad (8)$$

The fitting parameters and the χ^2 values over the number of degree-of-freedom (dof) are given in Table 3. We obtain a correlation slope of $\beta \sim 2.5 - 2.8$. The large scatter of the data around this relation indicates an intrinsic dispersion around the function. We estimate this dispersion by quadratically adding an intrinsic error, $\sigma_{\log(\tau)}^{\text{int}}$, to the statistical ones. Solving $\chi^2/\text{dof} \approx 1$, we obtain $\sigma_{\log(\tau)}^{\text{int}} \approx 0.20$ and 0.26 for the ACIS-I and -S/HETG0 data sets, respectively. However, we note that these estimates and fittings, obtained without proper accounting for the incompleteness and bias of the flare detection (§3.3), are for crude characterizations only. More rigorous treatments will be presented in a forthcoming work.

4.2 Quiescent emission

Fig. 6 presents the fitting count rates of the quiescent component for all the observations. This component includes the background emission, as well as the truly quiescent emission and contribution from undetected weak flares of Sgr A*. The difference between the mean ACIS-I and -S/HETG0 rates of the component is consistent with the effective area ratio of the two instrument setups (~ 2.6 ; see §3.5). We estimate the background count rates from nearby regions around Sgr A*, scaled to our aperture for the flare detection. The rates are about 1.00 cts ks^{-1} and 0.38 cts ks^{-1} for the ACIS-I and -S/HETG0 observations. Therefore, most of the fitting quiescent component actually comes from Sgr A* itself or other positionally overlapping sources. About 10% – 15% of this emission could be attributed to undetected weak flares assuming a simple fluence

distribution extrapolation from detected ones (Neilsen et al. 2015). Thus the truly quiescent emission accounts for the largest portion of this quiescent component.

We now examine the variation of the quiescent emission from Sgr A* on various time scales. First we check whether or not there is any significant change which might be attributed to the pericenter passages of the G1 cloud around the time of the year 2001.57 (Pfuhl et al. 2015) and S2 star around 2002.33 (Schödel et al. 2002). The ± 0.5 year intervals about the passages are shown in Fig. 6. While there was no observation during the interval around the G1 passage, 9 observations were around the S2 passage. No significant variation in the quiescent count rate during this latter interval is found compared with the 12-year average.

We also do not find any significant systematic trend in the quiescent count rate history, for either ACIS-I or -S/HETG0 observations. However, we do find significant rate variation among different observations (judging from the values of the best-fitting χ^2/dof). The intrinsic root-mean-square (RMS) fluctuation of the quiescent component, added quadratically to the Poisson errors, is estimated to be $\sim 14\%$ (6%) for the ACIS-I (-S/HETG0) data via setting $\chi^2/\text{dof} \sim 1$. To characterize the intrinsic non-flare variation, we need to account for various statistical fluctuations. The error bars in Fig. 6 only account for the counting statistics of the observed photon events. Additional fluctuations are expected from the limited number statistics of weak flares below our detection threshold in individual observations, which are particularly important in those with short exposures (e.g., the ACIS-I observations with ObsID 6640, 6641, 6642, 6645, 6646, and 7558). Therefore, the above RMSs represent only the upper limit to the true variation of the quiescent rate among the observations. Because the exposures of the ACIS-S/HETG0 observations are long, the fluctuation due to the number statistics of undetected weak flares is smaller, as shown by the $\sim 6\%$ intrinsic RMS.

4.3 Flare rate

The flare rate is another important statistical quantity related to the nature of the flares. The rate is estimated to be about 1.9 ± 0.3 or $1.4 \pm 0.2 \text{ day}^{-1}$ for the ACIS-I or -S/HETG0 observations. The intrinsic fluence (defined as fluence divided by area) detection limit of the ACIS-I flares is expected to be about 1.6 times lower than that of the -S/HETG0 ones⁶. According to the fluence distribution $N(>F) \propto F^{-0.5}$ (N13), the ACIS-I to -S/HETG0 flare rate ratio is expected to be ~ 1.3 , which is roughly consistent with the above detected rate difference. On the other hand, if taking the lowest intrinsic fluence of the ACIS-S/HETG0 flares as threshold, we find an ACIS-I to -S/HETG0 flare rate ratio of 0.9 ± 0.2 . The flare rates between these two data sets are consistent with each other.

To explore the systematic long-term change of the flare rate, we calculate the cumulative number of flares as a function of exposure time, as shown in the top panels of Fig. 7. The nearly linear increase of the number with time suggests that the flare rate is approximately constant during these observations. The KS tests show that the observations are consistent with the null hypothesis with high probabilities (see the statistic D and P_{KS} values inserted in the upper panels of Fig. 7).

The bottom panels of Fig. 7 show the (cumulative) waiting

⁶ The detected lowest intrinsic fluence of the ACIS-I flares is about 2.2 times lower than that of the -S/HETG0 ones, which is subject to uncertainty from the detection of faint flares (§3.3).

Table 1. Sgr A* flares detected in the ACIS-I data

ObsID	Date	Start (ks)	End (ks)	Exp. (ks)	κ (cts/ks)	FlrID	$\log(F/\text{cts})$	Peak (ks)	$\log(\tau/\text{ks})$	L_{2-8}^{unabs} (10^{34} erg/s)	N_{sub}	P	Ref.
242	1999-09-21	54270.275	54320.032	49.8	4.20 ± 0.30								
					fixed [‡]	I1	1.07 ± 0.23	54272.168	$0.45 \pm 0.20^{\dagger}$	0.30	1		(1)
1561	2000-10-26	88985.913	89022.169	36.3	4.46 ± 0.43	I2	1.35 ± 0.12	89001.653	0.03 ± 0.12	1.53	1		
						I3	2.95 ± 0.05	89011.674	0.93 ± 0.03	7.64	3	0.0067	(2),(3)
2951	2002-02-19	130517.00	130529.54	12.5	4.94 ± 0.73	I4	1.00 ± 0.26	130521.47	0.14 ± 0.29	0.53	1		
2952	2002-03-23	133274.58	133286.59	12.0	4.45 ± 0.65	I5	0.82 ± 0.30	133278.21	-0.04 ± 0.41	0.53	1		
2953	2002-04-19	135601.19	135612.93	11.7	4.09 ± 0.58								
2954	2002-05-07	137151.56	137164.17	12.6	4.58 ± 0.61								
2943	2002-05-22	138496.84	138535.02	38.2	4.35 ± 0.32								
3663	2002-05-24	138629.52	138667.99	38.5	5.38 ± 0.45	I6	1.85 ± 0.10	138656.20	0.80 ± 0.09	0.82	2	0.054	(3)
3392	2002-05-25	138728.07	138896.97	168.9	4.90 ± 0.18	I7	1.72 ± 0.09	138774.36	0.60 ± 0.11	0.96	1		(3)
						I8	1.02 ± 0.19	138782.73	0.01 ± 0.26	0.75	1		
						I9	1.49 ± 0.12	138808.50	0.64 ± 0.14	0.52	1		(3)
						I10	1.39 ± 0.12	138865.34	0.18 ± 0.09	1.18	1		(3)
						I11	1.09 ± 0.18	138878.91	0.23 ± 0.21	0.53	1		
3393	2002-05-28	138952.39	139112.51	160.1	4.80 ± 0.18	I12	2.53 ± 0.03	138987.68	0.52 ± 0.03	7.47	1		(3)
						I13	2.18 ± 0.07	139039.72	0.76 ± 0.10	1.92	2	0.059	(3)
						I14	1.85 ± 0.06	139085.21	0.15 ± 0.05	3.66	1		(3)
3665	2002-06-03	139455.69	139546.81	91.1	4.82 ± 0.23	I15	0.94 ± 0.24	139465.08	-0.14 ± 0.61	0.88	1		
3549	2003-06-19	172435.60	172460.71	25.1	5.04 ± 0.52	I16	1.17 ± 0.22	172453.77	0.47 ± 0.24	0.37	1		(4)
4683	2004-07-05	205454.84	205505.02	50.2	4.60 ± 0.30								
4684	2004-07-06	205541.03	205591.21	50.2	5.78 ± 0.34								
					fixed [‡]	I17	0.92 ± 0.21	205543.34	-0.20 ± 0.28	0.96	1		(5)
						I18	2.15 ± 0.05	205558.31	0.36 ± 0.04	4.50	1		(3),(5)
5360	2004-08-28	210082.80	210087.97	5.2	4.83 ± 0.95								
6113	2005-02-27	225874.38	225879.30	4.9	4.52 ± 0.94								
5950	2005-07-24	238623.22	238672.40	49.2	5.09 ± 0.33								
5951	2005-07-27	238879.92	238925.10	45.2	4.91 ± 0.35								
5952	2005-07-29	239054.88	239100.81	45.9	4.90 ± 0.38	I19	1.77 ± 0.08	239079.32	0.83 ± 0.09	0.64	1		(3),(6)
5953	2005-07-30	239141.35	239187.31	46.0	4.77 ± 0.35	I20	2.04 ± 0.05	239149.82	0.45 ± 0.06	2.84	1		(3),(7)
5954	2005-08-01	239314.38	239332.69	18.3	4.17 ± 0.50								
6639	2006-04-11	261121.70	261126.25	4.5	4.81 ± 0.99								
6640	2006-05-03	263083.36	263088.53	5.2	7.50 ± 1.22								
6641	2006-06-01	265566.30	265571.42	5.1	8.96 ± 1.30								
					fixed [‡]	I21	1.15 ± 0.17	265567.89	0.30 ± 0.21	0.52	1		
6642	2006-07-04	268399.23	268404.41	5.2	7.57 ± 1.17								
6363	2006-07-17	269496.92	269527.08	30.2	4.13 ± 0.41								
					fixed [‡]	I22	2.24 ± 0.05	269503.80	0.41 ± 0.03	4.94	1		(3),(7),(8)
6643	2006-07-30	270657.94	270662.98	5.0	4.55 ± 0.91								
6644	2006-08-22	272614.20	272619.24	5.0	5.68 ± 1.03								
6645	2006-09-25	275580.29	275585.47	5.2	8.02 ± 1.19								
					fixed [‡]	I23	1.07 ± 0.19	275581.21	$0.32 \pm 0.16^{\dagger}$	0.41	1		
6646	2006-10-29	278480.67	278485.84	5.2	7.70 ± 1.13								
7554	2007-02-11	287562.96	287568.11	5.1	4.28 ± 0.94								
7555	2007-03-25	291251.43	291256.59	5.2	5.74 ± 1.07								
7556	2007-05-17	295752.54	295757.58	5.0	5.83 ± 1.00								
7557	2007-07-20	301287.05	301292.10	5.0	5.37 ± 1.07								
7558	2007-09-02	305152.60	305157.65	5.0	9.38 ± 1.43								
					fixed [‡]	I24	1.14 ± 0.15	305153.70	0.30 ± 0.16	0.51	1		
7559	2007-10-26	309781.44	309786.51	5.1	5.35 ± 1.01								
9169	2008-05-05	326348.29	326376.24	28.0	5.71 ± 0.47								
					fixed [‡]	I25	0.99 ± 0.26	326371.05	-0.49 ± 0.51	2.20	1		(3),(9)
9170	2008-05-06	326431.43	326458.58	27.1	5.23 ± 0.42								
9171	2008-05-10	326777.71	326805.76	28.0	4.87 ± 0.39								
9172	2008-05-11	326865.44	326893.23	27.8	5.38 ± 0.43								
9174	2008-07-25	333410.76	333439.94	29.2	4.46 ± 0.39								
9173	2008-07-26	333495.51	333523.64	28.1	4.11 ± 0.52								
					fixed [‡]	I26	1.14 ± 0.21	333499.49	0.51 ± 0.26	0.31	1		
						I27	1.21 ± 0.18	333504.75	0.36 ± 0.26	0.52	1		(9)
10556	2009-05-18	359001.57	359115.62	114.1	4.71 ± 0.22	I28	1.78 ± 0.12	359002.25	$0.55 \pm 0.19^{\dagger}$	1.24	2	0.048	(3)
						I29	1.90 ± 0.12	359029.24	0.61 ± 0.09	1.42	2	0.049	(3),(10)
						I30	2.34 ± 0.05	359075.91	0.28 ± 0.03	8.38	1		(3)
						I31	1.79 ± 0.09	359081.83	-0.12 ± 0.07	5.93	1		(3)
11843	2010-05-13	390104.87	390184.84	80.0	5.52 ± 0.27								
					fixed [‡]	I32	2.73 ± 0.04	390110.65	0.58 ± 0.02	10.3	1		(3)
13016	2011-03-29	417782.70	417800.76	18.1	3.33 ± 0.50								
					fixed [‡]	I33	1.28 ± 0.14	417783.64	$0.39 \pm 0.13^{\dagger}$	0.57	1		(3)
13017	2011-03-31	417955.49	417973.56	18.1	4.49 ± 0.52								

Note: Columns from left to right are: observation ID, observing date, starting time and ending time from UT 1998-01-01 00:00:00, exposure, quiescent count rate, flare ID, logarithmic fluence, peak time, logarithmic duration, mean unabsorbed 2 – 8 keV luminosity within the duration, number of subflares, the chance probability of uncorrelated flares overlapping with the main flare, and the references of previous works. Posterior marginalized 1σ errors are included for the fluence and the duration.

[†]Flare truncated by the starting or ending of an observation.

[‡]Quiescent emission is fixed at 4.86 cts ks^{-1} — the mean rate of all the ACIS-I observations.

References: (1) Baganoff et al. (2003); (2) Baganoff et al. (2001); (3) Ponti et al. (2015); (4) Eckart et al. (2004); (5) Eckart et al. (2006a); (6) Eckart et al. (2008); (7) Hornstein et al. (2007); (8) Marrone et al. (2008); (9) Yusef-Zadeh et al. (2012); (10) Eckart et al. (2012).

Table 2. Sgr A* flares detected in the ACIS-S/HETG0 data

ObsID	Date	Start (ks)	End (ks)	Exp. (ks)	κ (cts/ks)	FlrID	$\log(F/\text{cts})$	Peak (ks)	$\log(\tau/\text{ks})$	$L_{\text{unabs}}^{\text{2-8}}_{\text{2-8}}$ (10^{34} erg/s)	N_{sub}	P	Ref.
13850	2012-02-06	444877.14	444937.14	60.0	1.68 ± 0.16								
14392	2012-02-09	445156.63	445215.88	59.2	1.80 ± 0.19	S1	1.18 ± 0.13	445171.72	0.27 ± 0.14	1.53	1		(1),(2)
						S2	2.75 ± 0.03	445187.73	0.71 ± 0.02	20.6	1		(1),(2)
14394	2012-02-10	445232.14	445250.21	18.1	2.45 ± 0.38								
14393	2012-02-11	445343.58	445385.13	41.5	2.38 ± 0.24								
13856	2012-03-15	448189.56	448229.62	40.1	1.62 ± 0.21								
13857	2012-03-17	448363.06	448402.61	39.6	2.22 ± 0.23								
13854	2012-03-20	448626.68	448649.75	23.1	2.09 ± 0.35	S3	1.37 ± 0.11	448631.25	-0.10 ± 0.09	5.55	1		(2)
						S4	1.38 ± 0.11	448634.81	0.12 ± 0.10	3.42	1		(2)
						S5	1.37 ± 0.11	448639.76	0.19 ± 0.10	2.85	1		(2)
						S6	1.51 ± 0.09	448647.98	-0.18 ± 0.08	9.21	1		(2)
14413	2012-03-21	448700.54	448715.26	14.7	1.72 ± 0.32								
13855	2012-03-22	448803.91	448823.97	20.1	2.11 ± 0.31								
14414	2012-03-23	448913.21	448933.27	20.1	1.84 ± 0.32								
13847	2012-04-30	452191.00	452345.06	154.1	1.88 ± 0.11	S7	1.55 ± 0.08	452263.05	0.59 ± 0.08	1.71	1		(2)
14427	2012-05-06	452722.87	452802.93	80.1	1.74 ± 0.16	S8	1.43 ± 0.11	452747.93	0.40 ± 0.14	2.01	1		(2)
						S9	1.36 ± 0.11	452777.65	0.67 ± 0.13	0.92	1		
13848	2012-05-09	452953.42	453051.58	98.2	1.88 ± 0.14								
13849	2012-05-11	453095.24	453273.98	178.7	1.96 ± 0.12	S10	1.41 ± 0.18	453141.81	0.86 ± 0.58	0.67	2	0.058	(2)
						S11	1.27 ± 0.12	453170.73	0.47 ± 0.13	1.19	1		(2)
						S12	1.10 ± 0.21	453195.75	0.64 ± 0.32	0.54	1		(2)
						S13	1.94 ± 0.05	453267.26	0.49 ± 0.05	5.30	1		(2)
13846	2012-05-16	453552.19	453607.19	55.0	1.54 ± 0.17								
14438	2012-05-18	453703.94	453729.73	25.8	1.93 ± 0.27								
13845	2012-05-19	453812.55	453947.86	135.3	1.66 ± 0.12								
					fixed [‡]	S14	1.00 ± 0.18	453823.23	0.32 ± 0.19	0.90	1		
						S15	1.82 ± 0.11	453935.16	0.30 ± 0.10	6.23	2	0.012	(2)
						S16	1.11 ± 0.15	453938.91	0.20 ± 0.15	1.53	1		
						S17	1.06 ± 0.17	453946.43	$0.47 \pm 0.15^{\dagger}$	0.73	1		
14460	2012-07-09	458261.60	458285.66	24.1	2.54 ± 0.30								
13844	2012-07-10	458351.01	458371.07	20.1	1.81 ± 0.30								
14461	2012-07-12	458459.40	458510.37	51.0	1.75 ± 0.18								
13853	2012-07-14	458613.56	458687.22	73.7	1.84 ± 0.16								
13841	2012-07-17	458947.94	458993.01	45.1	1.90 ± 0.21								
14465	2012-07-18	459041.14	459085.48	44.3	1.79 ± 0.23	S18	1.56 ± 0.08	459043.46	$0.74 \pm 0.07^{\dagger}$	1.24	1		(2)
						S19	1.16 ± 0.14	459059.71	0.43 ± 0.12	1.01	1		(2)
14466	2012-07-20	459176.36	459221.44	45.1	2.21 ± 0.24								
					fixed [‡]	S20	1.39 ± 0.11	459177.21	0.09 ± 0.14	3.75	1		(2)
						S21	1.03 ± 0.15	459217.78	-0.09 ± 0.14	2.48	1		
13842	2012-07-21	459260.69	459452.44	191.8	1.89 ± 0.11	S22	1.85 ± 0.06	459320.36	0.59 ± 0.05	3.42	1		(2)
						S23	1.36 ± 0.11	459381.31	0.02 ± 0.10	4.11	1		(2)
						S24	1.85 ± 0.09	459437.62	0.94 ± 0.08	1.53	2	0.039	(2)
13839	2012-07-24	459501.75	459678.00	176.3	1.84 ± 0.11	S25	1.47 ± 0.09	459509.11	0.04 ± 0.08	5.06	1		(2)
						S26	0.95 ± 0.18	459606.20	-0.29 ± 0.19	3.27	1		(2)
						S27	2.27 ± 0.04	459649.70	0.57 ± 0.03	9.42	1		(2)
13840	2012-07-26	459721.42	459883.94	162.5	2.00 ± 0.12	S28	1.27 ± 0.13	459863.37	0.55 ± 0.14	0.99	1		
						S29	0.96 ± 0.28	459876.27	0.55 ± 0.33	0.48	1		
14432	2012-07-30	460041.72	460115.99	74.3	1.61 ± 0.16								
					fixed [‡]	S30	1.41 ± 0.10	460044.94	$0.73 \pm 0.09^{\dagger}$	0.90	1		
						S31	2.09 ± 0.04	460113.72	$0.60 \pm 0.03^{\dagger}$	5.81	1		(2)
13838	2012-08-01	460230.82	460330.38	99.6	2.01 ± 0.15	S32	2.01 ± 0.08	460254.74	0.51 ± 0.11	5.95	2	0.034	(2)
						S33	0.86 ± 0.20	460269.49	-0.05 ± 0.23	1.53	1		
13852	2012-08-04	460436.77	460593.34	156.6	1.68 ± 0.11								
					fixed [‡]	S34	1.60 ± 0.08	460453.54	0.13 ± 0.05	5.55	1		(2)
						S35	1.57 ± 0.10	460495.90	1.24 ± 0.09	0.40	1		
						S36	1.37 ± 0.10	460541.81	0.52 ± 0.13	1.33	1		(2)
14439	2012-08-06	460679.74	460791.48	111.7	2.02 ± 0.14	S37	1.30 ± 0.12	460783.48	0.40 ± 0.13	1.49	1		(2)
14462	2012-10-06	465929.41	466063.49	134.1	1.87 ± 0.12	S38	1.22 ± 0.15	465971.27	0.54 ± 0.17	0.90	1		(2)
						S39	1.40 ± 0.10	466058.86	0.38 ± 0.09	1.97	1		(2)
14463	2012-10-16	466737.09	466767.86	30.8	2.61 ± 0.28								
					fixed [‡]	S40	1.68 ± 0.08	466753.89	-0.09 ± 0.07	11.1	1		(2)
13851	2012-10-16	466802.39	466909.45	107.1	2.03 ± 0.14	S41	0.74 ± 0.24	466827.54	-0.14 ± 0.25	1.43	1		(2)
						S42	2.38 ± 0.05	466891.41	0.68 ± 0.08	9.42	2	0.043	(2)
15568	2012-10-18	466938.99	466975.06	36.1	1.51 ± 0.24								
					fixed [‡]	S43	1.20 ± 0.13	466972.41	0.34 ± 0.19	1.36	1		
13843	2012-10-22	467310.03	467430.71	120.7	1.96 ± 0.14	S44	2.24 ± 0.06	467372.68	0.82 ± 0.10	4.94	2	0.072	(2)
						S45	1.19 ± 0.24	467418.81	0.88 ± 0.34	0.38	1		
15570	2012-10-25	467524.25	467592.96	68.7	1.71 ± 0.16	S46	1.59 ± 0.12	467532.67	0.38 ± 0.10	3.05	2	0.025	(2)
14468	2012-10-29	467943.30	468089.36	146.1	1.78 ± 0.11	S47	1.66 ± 0.08	467970.68	0.84 ± 0.10	1.24	1		(2)
						S48	0.83 ± 0.19	468005.49	-0.03 ± 0.19	1.36	1		(2)
						S49	1.49 ± 0.10	468079.07	0.51 ± 0.14	1.80	1		(2)

Note: Same as Table 1.

[†]Flare is truncated by the start or end of an observation.[‡]Quiescent emission is fixed to be 1.86 cts ks^{-1} .

References: (1) Nowak et al. (2012); (2) Neilsen et al. (2013).

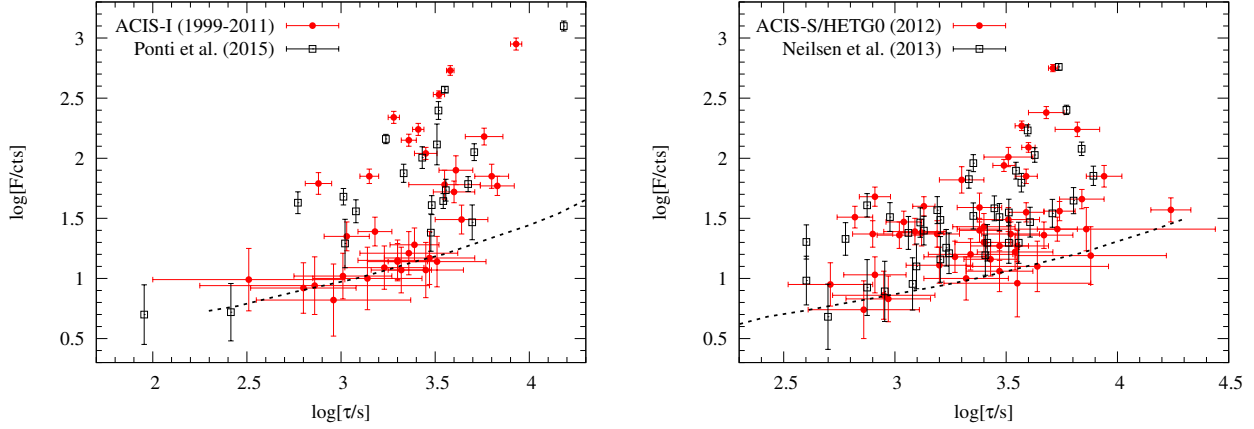


Figure 5. Fluence versus duration distribution of the detected flares for the ACIS-I (left) and -S/HETG0 (right) observations. The results of P15 and N13 are also shown for comparison. The dotted lines show the 50% incompleteness limit of our flare detections (Fig. 3).

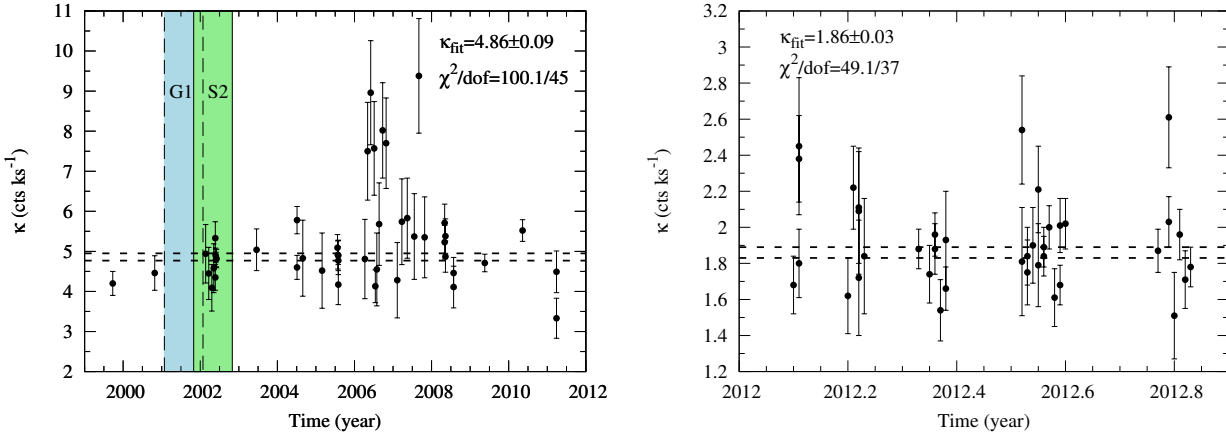


Figure 6. The quiescent emission rate of Sgr A* as a function of the date for the ACIS-I (left) and ACIS-S/HETG0 (right) observations. The horizontal lines mark the $\pm 1\sigma$ range of the constant fittings. Shaded regions in the left panel show the ± 0.5 year around the best-fitting pericenter passages of the G1 cloud (Pfuhl et al. 2015) and S2 star (Schödel et al. 2002).

Table 3. Fitting results of the flare fluence-duration correlations

	$\log(\alpha)$	β	χ^2/dof	$\sigma_{\log(\tau)}^{\text{int}}$
ACIS-I	1.14 ± 0.08	2.45 ± 0.16	239.8/31	0.20
P15	1.70 ± 0.03	1.05 ± 0.04	609.0/18	
ACIS-S/HETG0	0.56 ± 0.09	2.78 ± 0.17	392.9/47	0.26
N13	1.54 ± 0.03	1.26 ± 0.05	562.1/37	

time distributions of the consecutive flares in individual observations, observed and expected for non-clustering hypothesis (see Eq. (7) in § 3.4). Deviations from the expectations of the null hypothesis, consistently occurring on time scales of ~ 40 ks for both the ACIS-I and -S/HETG0 flare samples, can be seen in these plots, although only the deviation in the latter sample is significant at the 96% confidence, according to the KS test. The clustering is less significant for the ACIS-I flare sample, apparently due to its smaller size⁷. The presence of this short-term clustering may sug-

gest that X-ray flares of Sgr A* mimic the foreshock or after-shock of earthquakes, which can be described with a piecewise-deterministic Markov process (Davis 1984).

5 COMPARISON WITH PREVIOUS WORKS

We now compare our results about the flares with those of P15 (for the ACIS-I data) and N13 (for the ACIS-S/HETG0 data). Based on the same ACIS-I observations, 19 flares are jointly detected in our analysis and in P15, which are shown in the top-left panel of Fig. 8. There are quite a few apparent discrepancies in the flare parameters between these two analyses. In particular, the fluences derived in P15 seem to be systematically lower and the durations are systematically shorter than ours. Such differences may be expected from the different analysis methods and definitions of the flare parameters adopted in the analyses. In P15 the Bayesian block method (Scargle 1998) was adopted to detect flares, while the likelihood fitting method is used in our analysis. The flare duration was defined as the first and last of the significant change points characterizing the flaring blocks, which is different from our definition of the 95% emission window. Typically, the Bayesian block method

⁷ Note that the D values are comparable for the two samples (Fig. 7).

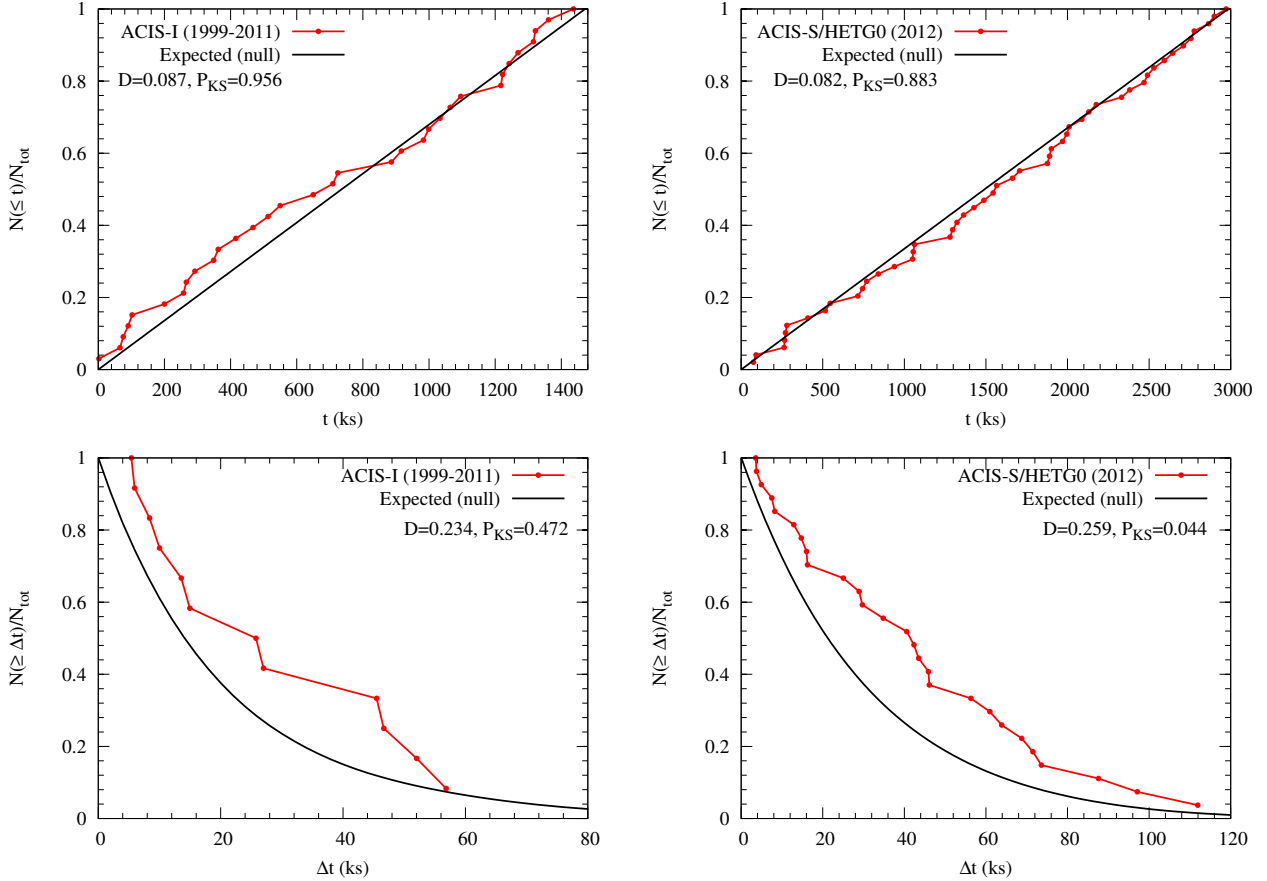


Figure 7. Top panels: normalized backward cumulative number $N(\leq t)/N_{\text{tot}}$ of flares versus the accumulated exposure time. The red thick lines with dots represent the results from the real observational data, while the black lines show linear behaviors expected from random occurrence of flares (null hypothesis) with constant flare rates: $f \approx 1.9 \text{ day}^{-1}$ for the ACIS-I observations (left) and $f \approx 1.4 \text{ day}^{-1}$ for the ACIS-S/HETG0 observations (right). Bottom panels: normalized forward cumulative number $N(\geq \Delta t)/N_{\text{tot}}$ of flares versus the waiting time since the preceding one. The expected distributions for null hypothesis (black solid lines) are calculated according to Eq. (7).

tends to systematically underestimate the count rate and duration of a flare because only detected flaring blocks are counted. For flares with significant substructures (e.g., FlrID I3), however, the Bayesian block method tends to give longer durations than our definition. Compared with P15, we detect 14 more flares and miss 1 flare (bottom-left panel of Fig. 8). Most of these flares are weak and just above the detection threshold.

For the ACIS-S/HETG observations, N13 detected 39 flares using the binned 0th+1st order lightcurves and a different likelihood fitting method. Thirty-seven flares are common in their analysis and ours (top-right panel of Fig. 8). Here the fluences of N13 flares have been multiplied by a factor of ~ 0.6 to account for the difference of the data selection. Also the pileup effect on N13 flares has been corrected. The results of the common sample between these two analyses are mostly consistent with each other within the errorbars. Note that a few flares in the N13 sample have durations which are comparable to their adopted bin width (300 s) and are likely very uncertain. Furthermore, the duration of an N13 flare with subflares is defined as the total interval between their lowest and highest 2σ limits, in contrast to our definition as the 95% emission-enclosed time interval. Two N13 flares are not detected, whereas 12 more are detected in our re-analysis of the ACIS-S/HETG0 data. All these flares are faint (see the bottom-right panel of Fig. 8), sensitive to the difference in the analysis methods.

An alternative method, the Bayesian block algorithm, was tested in N13, which returned a set of 45 flares, whereas P15 detected 37 flares using the 0th order data of the 2012 XVP observations with the same method.

In both analyses of the ACIS-I and -S/HETG0 data, we detect a number of new flares with relatively low fluences and long durations. The detection of these flares are justified with the expected sensitivity (the incompleteness curve) of our improved detection method.

We also perform fittings to the fluence-duration correlation for the P15 and N13 flare samples, with only the fluence errors considered, as shown in Table 3. The correlation slope β is much smaller than the values from the fitting to our samples (§4.1). This is mostly due to our inclusion of the uncertainties in the duration measurements, which affects the weights of individual flares in the χ^2 fitting. Li et al. (2015) studied the flare statistics through a joint fitting to the count rate distribution and structure function of the XVP lightcurve, and found that $\beta > 1.8$ at the 95% confidence level, consistent with our results.

P15 studied the flare rate in the past 15 years with the *Chandra* and *XMM-Newton* observations. They found that the flare rate before 2013 did not change significantly, which is consistent with our result. However, the bright flare rate showed evidence for a significant increase by a factor of ~ 10 starting from August 2014, which

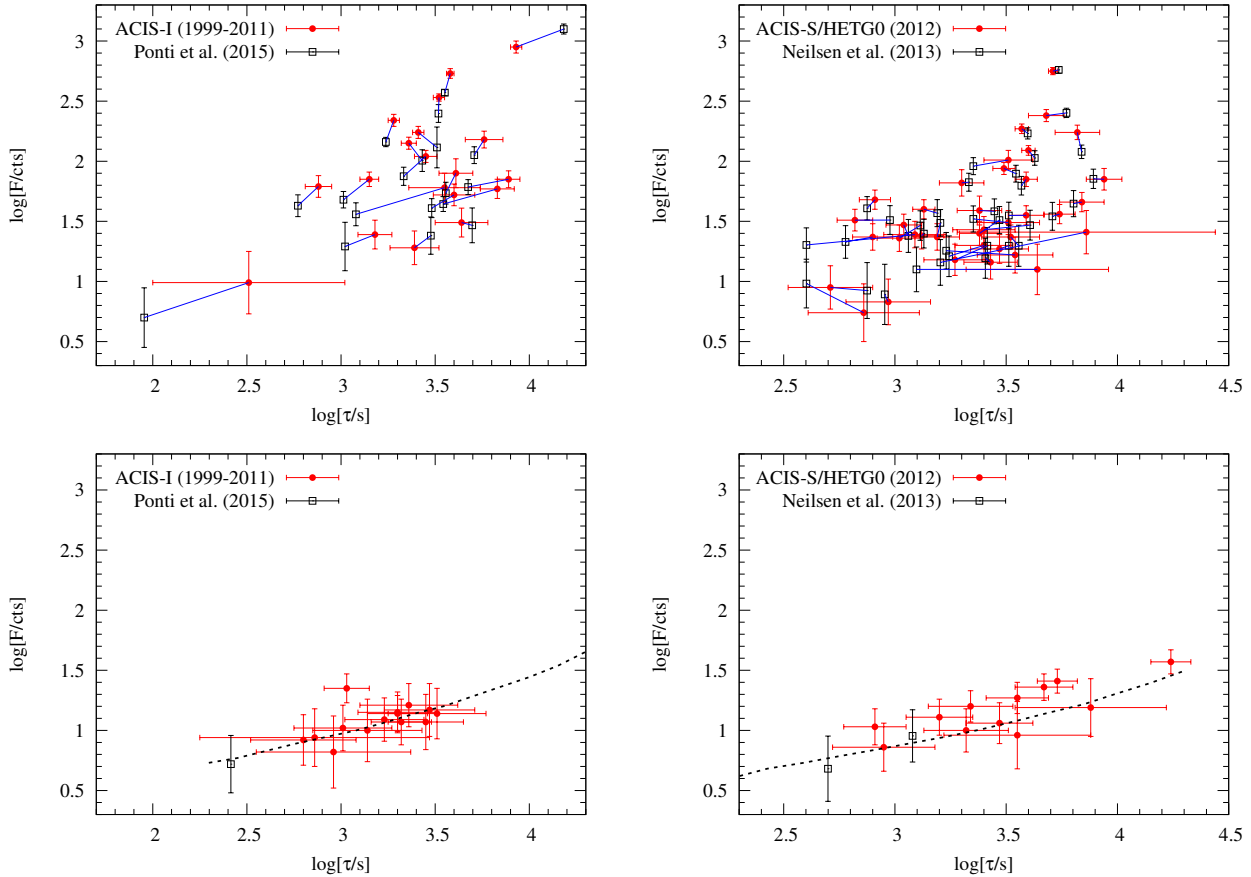


Figure 8. Top panels: comparisons of the fluence-duration distributions of the flares commonly detected in the present work, as well as in P15 for the ACIS-I observations (left) or N13 for the ACIS-S/HETG0 observations (right). Bottom panels: same as the top ones but for the flares detected only in our analysis or P15/N13 analysis. The dotted lines are the 50% incompleteness limits as in Fig. 5.

happened to be about half year after the G2’s pericenter passage (Gillessen et al. 2013). We can check if a similar enhancement occurred after the S2 star’s pericenter passage. The 9 ACIS-I observations were taken in 2002 (with ObsID from 2951 to 3665), covering the period of the passage around 2002.33. In total we find 12 flares in 545.6 ks exposure, which corresponds to a flare rate of $\sim 1.9 \text{ day}^{-1}$, well consistent with the 12 years’ average. The number of bright flares (each with > 120 cts, corresponding to the definition of bright flares for the ACIS-I observations in P15) in the 2002 observations is 2. Compared with the total number of bright flares of 7 in all the ACIS-I observations, no significant anomaly is shown in the bright flare rate, considering the exposure fraction (0.37) of the 2002 observations. The 3σ upper limit of the expected number of bright flares when detecting 2 flares is 10.9, which corresponds to a rate of 1.7 day^{-1} , about 4 times higher than the average one ($7/1.47 \text{ Ms}^{-1} \approx 0.4 \text{ day}^{-1}$) in all the ACIS-I observations. A 10 times enhancement of the bright flare rate associated with the S2’s pericenter passage, similar to that found in P15 during the G2’s passage, can thus be excluded.

All these differences demonstrate the importance to enlarge the sample size and dynamic range of X-ray flares, and to carefully address their detection incompleteness and bias, as well as the parameter measurement uncertainties, as are achieved in the present work. As a result, we are now in a good position to provide a significantly improved assessment of the statistical properties of the flaring phenomenon of Sgr A*.

6 SUMMARY

In this work we have systematically analyzed the *Chandra* lightcurves of Sgr A* from 1999 to 2012, including 46 ACIS-I and 38 ACIS-S/HETG0 observations. Our analysis uses a combination of the unbinned maximum likelihood fitting algorithm and the MCMC method, which enables us to maximize the use of information in the data and to estimate the uncertainties in all flare parameter measurements. This forward-fitting procedure also allows us to account for the pileup effect directly in the lightcurve modeling. This removes a big uncertainty in such a correction when it is applied to a flare without accounting for its shape. We have further carried out simple variability analyses of the detected flare rate and the quiescent emission. Our major results and conclusions are as follows:

- We detect 33 (49) flares in the ACIS-I (-S/HETG0) data. The bulk of these flares overlap with those reported in existing studies (P15 and N13). We give not only improved measurements of the parameters (including the first error estimates for the flare durations), but also a careful characterization of the detection incompleteness and bias. Our detections further reveal a number of faint flares (some of which have unusually long durations), which are missed in the existing studies. This discovery becomes possible due to the improved fitting method which allows for a more complete survey of the flare parameter space.
- Our analysis confirms the correlation of the flare fluence ver-

sus the duration, and gives new estimates of the mean relation $\log F = \log(\alpha) + \beta \log(\tau)$, for both ACIS-I and -S/HETG0 flare samples. A direct fitting to the measurements, accounting for the uncertainties in both $\log F$ and $\log \tau$, gives $\beta \sim 2.5 - 2.8$ for the two samples, which is significantly larger than that obtained with the N13 and P15 samples, but is consistent with that in Li et al. (2015). We further estimate an intrinsic dispersion of $\log(\tau) \sim 0.20 - 0.26$ around this relation.

- We do not find any significant long-term variation in the quiescent emission or the flare rate. In particular, no enhanced flare rate or quiescent emission is evident during the pericenter passage of the S2 star in 2002 (Schödel et al. 2002). The 3σ upper limit to the bright flare rate around S2's pericenter passage is about 4 times of the average rate for the entire ACIS-I flare sample, which rules out a factor of ~ 10 increase in the bright flare rate similar to that observed after the G2's passage (P15). The intrinsic RMS variation of the quiescent emission among the ACIS-I (-S/HETG0) observations is 14% (6%), part of which is expected from the number fluctuation of weak flares below our detection limits. The mean quiescent emissions and flare rates in the ACIS-I and -S/HETG0 observations are consistent with each other, when their effective area difference is accounted for.

- The flares seem to cluster on the time scale of 20 – 70 ks, particularly significant in the ACIS-S/HETG0 sample. This short-term clustering, as well as the non-variation of the long-term flare rate, suggests that the production of the flares may be described by a piecewise-deterministic Markov process (similar to that used to characterize earthquakes; Davis 1984), which deserves further in-depth analysis and modeling.

- The detection incompleteness and the redistribution matrix of the measured parameters are obtained through Monte Carlo simulations, enabling further statistical studies of the flares.

In a subsequent paper, we will present a rigorous statistical analysis of the flares (e.g., their fluence-duration relation), based on the characterization of the detection incompleteness and bias, as well as the error measurements of flare parameters as presented here. We will further examine the profiles (substructures and asymmetry) and phase-resolved spectra of the flares to shed light into their nature.

ACKNOWLEDGMENTS

We thank Shawn Roberts for helpful comments on the manuscript, and the referee for a careful reading and a useful review report.

REFERENCES

Arnaud K. A., 1996, in *Astronomical Society of the Pacific Conference Series*, Vol. 101, *Astronomical Data Analysis Software and Systems V*, Jacoby G. H., Barnes J., eds., p. 17
 Baganoff F. K. et al., 2001, *Nature*, 413, 45
 Baganoff F. K. et al., 2003, *ApJ*, 591, 891
 Bak P., Tang C., Wiesenfeld K., 1987, *Physical Review Letters*, 59, 381
 Barrière N. M. et al., 2014, *ApJ*, 786, 46
 Bélanger G., Goldwurm A., Melia F., Ferrando P., Grosso N., Porquet D., Warwick R., Yusef-Zadeh F., 2005, *ApJ*, 635, 1095
 Cash W., 1979, *ApJ*, 228, 939
 Davis M. H. A., 1984, *Journal of the Royal Statistical Society. Series B*, 46, 353

Degenaar N., Miller J. M., Kennea J., Gehrels N., Reynolds M. T., Wijnands R., 2013, *ApJ*, 769, 155
 Dodds-Eden K. et al., 2009, *ApJ*, 698, 676
 Dodds-Eden K., Sharma P., Quataert E., Genzel R., Gillessen S., Eisenhauer F., Porquet D., 2010, *ApJ*, 725, 450
 Eckart A. et al., 2004, *A&A*, 427, 1
 Eckart A. et al., 2006a, *A&A*, 450, 535
 Eckart A. et al., 2008, *A&A*, 479, 625
 Eckart A. et al., 2012, *A&A*, 537, A52
 Eckart A., Schödel R., Meyer L., Trippe S., Ott T., Genzel R., 2006b, *A&A*, 455, 1
 Gamerman D., 1997, *Markov Chain Monte Carlo: Stochastic Simulation for Bayesian Inference*. Chapman and Hall, London
 Genzel R., Schödel R., Ott T., Eckart A., Alexander T., Lacombe F., Rouan D., Aschenbach B., 2003, *Nature*, 425, 934
 Gillessen S. et al., 2013, *ApJ*, 774, 44
 Hornstein S. D., Matthews K., Ghez A. M., Lu J. R., Morris M., Becklin E. E., Rafelski M., Baganoff F. K., 2007, *ApJ*, 667, 900
 Katz J. I., 1986, *Journal of Geophysics Research*, 91, 10412
 Kennea J. A. et al., 2013, *ApJ*, 770, L24
 Kenter A. T., Murray S. S., 2003, *ApJ*, 584, 1016
 Kostić U., Čadež A., Calvani M., Gomboc A., 2009, *A&A*, 496, 307
 Li Y.-P. et al., 2015, *ApJ*, 810, 19
 Liu S., Melia F., 2002, *ApJ*, 566, L77
 Liu S., Melia F., Petrosian V., 2006, *ApJ*, 636, 798
 Liu S., Petrosian V., Melia F., 2004, *ApJ*, 611, L101
 Mackay D. J. C., 2003, *Information Theory, Inference and Learning Algorithms*. Cambridge University Press
 Markoff S., Falcke H., Yuan F., Biermann P. L., 2001, *A&A*, 379, L13
 Marrone D. P. et al., 2008, *ApJ*, 682, 373
 Mattox J. R. et al., 1996, *ApJ*, 461, 396
 Melia F., Falcke H., 2001, *ARA&A*, 39, 309
 Neal R. M., 1993, *Probabilistic Inference Using Markov Chain Monte Carlo Methods*. Department of Computer Science, University of Toronto
 Neilsen J. et al., 2015, *ApJ*, 799, 199
 Neilsen J. et al., 2013, *ApJ*, 774, 42
 Nowak M. A. et al., 2012, *ApJ*, 759, 95
 Pfuhl O. et al., 2015, *ApJ*, 798, 111
 Ponti G. et al., 2015, *MNRAS*, 454, 1525
 Porquet D. et al., 2008, *A&A*, 488, 549
 Porquet D., Predehl P., Aschenbach B., Grosso N., Goldwurm A., Goldoni P., Warwick R. S., Decourchelle A., 2003, *A&A*, 407, L17
 Scargle J. D., 1998, *ApJ*, 504, 405
 Schödel R. et al., 2002, *Nature*, 419, 694
 Trap G. et al., 2011, *A&A*, 528, A140
 Wang F. Y., Dai Z. G., Yi S. X., Xi S. Q., 2015, *ApJS*, 216, 8
 Wang Q. D., 2004, *ApJ*, 612, 159
 Wang Q. D. et al., 2013, *Science*, 341, 981
 Witzel G. et al., 2012, *ApJS*, 203, 18
 Yuan F., Lin J., Wu K., Ho L. C., 2009, *MNRAS*, 395, 2183
 Yuan F., Narayan R., 2014, *ARA&A*, 52, 529
 Yuan F., Quataert E., Narayan R., 2003, *ApJ*, 598, 301
 Yuan F., Quataert E., Narayan R., 2004, *ApJ*, 606, 894
 Yusef-Zadeh F. et al., 2012, *AJ*, 144, 1
 Yusef-Zadeh F., Wardle M., Heinke C., Dowell C. D., Roberts D., Baganoff F. K., Cotton W., 2008, *ApJ*, 682, 361
 Zubovas K., Nayakshin S., Markoff S., 2012, *MNRAS*, 421, 1315

**APPENDIX A: LIGHTCURVES OF ALL THE DETECTED
FLARES**

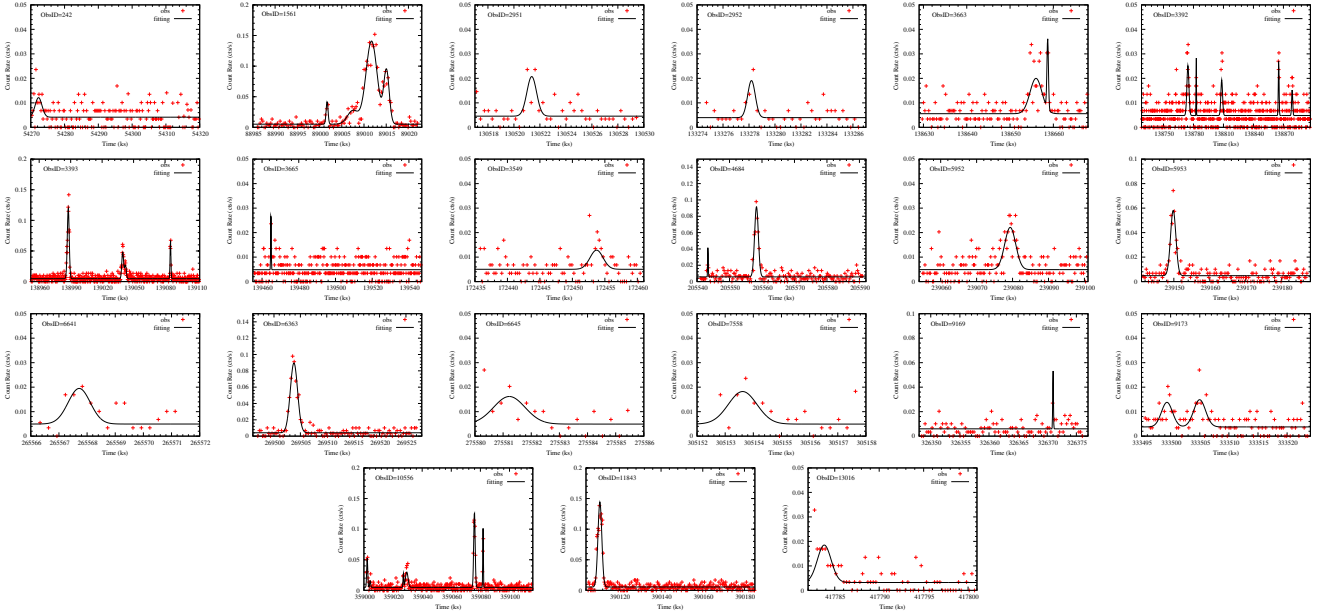


Figure A1. Lightcurves of the detected flares in the *Chandra* ACIS-I observations, compared with the best-fitting results.

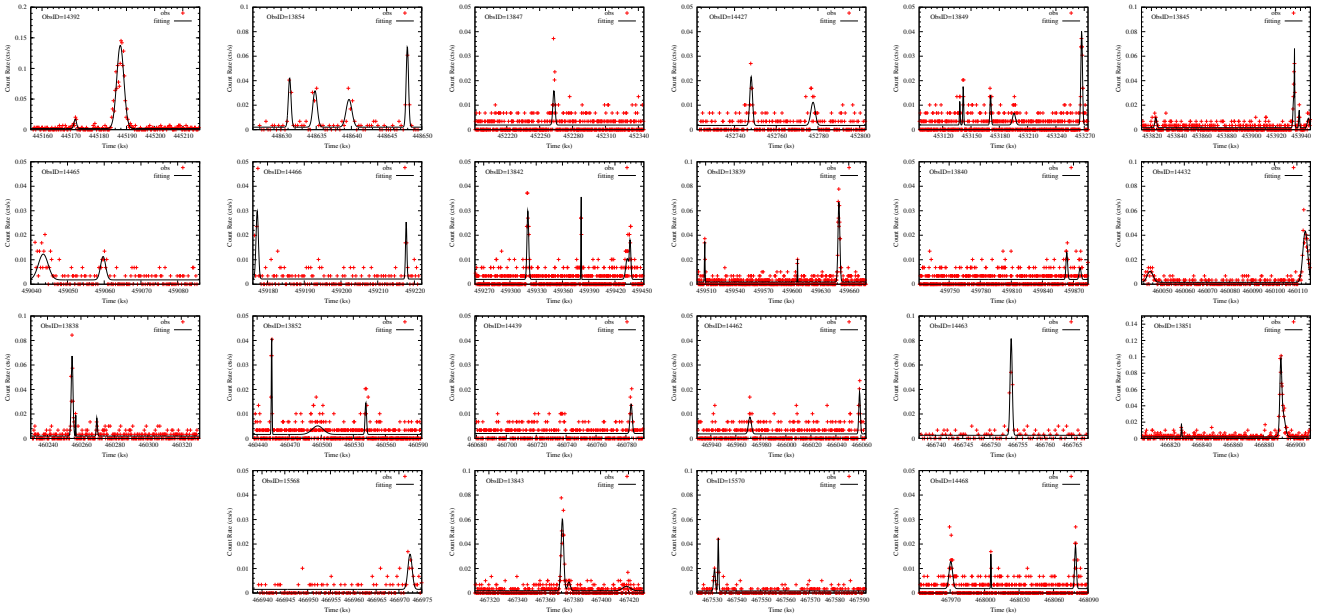


Figure A2. Lightcurves of the detected flares in the *Chandra* ACIS-S/HETG observations, compared with the best-fitting results.